Complex Permittivity Retrieval Approach With Radar Enhanced Contrast Source Inversion for Microwave Nondestructive Road Evaluation

Katsuyoshi Suzuki, Shingo Nakamura, and Shouhei Kidera, *Senior Member, IEEE*

***Abstract*—In this article, an experimental investigation of microwave quantitative imaging of nondestructive testing (NDT) applications for concrete road structures is presented. A radar prior-based contrast source inversion (CSI) scheme is introduced to achieve an accurate reconstruction for target shape and dielectric property by applying the promising radar approach–range points migration. Moreover, to address the local optimum problem, we introduce an appropriate initial estimate for complex permittivity that focuses on the cost function of the CSI. A numerical and real data from an actual concrete road model, where a thin-layer water-filled cavity is buried into the boundary area between the asphalt and the concrete floorboard, show that our proposed approach improves reconstruction accuracy for permittivity and conductivity in a real NDT model.**

***Index Terms*—Contrast source inversion (CSI), inverse scattering analysis, microwave quantitative imaging, nondestructive testing (NDT) for concrete road, range points migration (RPM).**

I. Introduction

DEMANDS for emergent monitoring of aging roads, tunnels, bridges, or other transportation infrastructures are increasing, and a speedy and accurate nondestructive testing (NDT) technique is strongly required for anomaly detection, such as corrosion of reinforced rod, water leakage into air crack, or chloride ingress. One of the promising solutions for the above application is microwave-based nondestructive evaluation (MWNDE) radar, which retains sufficient penetration depth (exceeding 500 mm) and high-depth resolutions while significantly reducing labor costs and time for large-scale inspection [1], [2], [3].

The radar approach, a major imaging scheme for MWNDE, which is based on the coherent synthesis of recorded signals with array or scanning, provides us with the location or shape of buried objects with high dielectric contrast from background media, such as air, water cavity, or metallic pipe [1], [4]. In [5] and [6], TOF-based incoherent imaging approaches have been developed to more accurately reconstruct target shapes using point cloud expressions. Among these methods, the range points migration (RPM) method offers several advantages, such as low complexity and high accuracy for complex-shaped objects [5], [7]. However, the radar-based approach cannot provide quantitative reconstruction for dielectric profiles, such as permittivity and conductivity, creating a significant challenge in determining the material property of buried objects. To be more specific, focusing on road inspection, a water leakage accumulating in an area between asphalt and floorboard would be fatal for road strength degradation, possibly causing subsidence; however, the radar-based approach could not classify whether the focused image would be air crack or water leakage. Several trends use machine learning approaches to detect anomalies in rebar, such as corrosion. These are evident in methods that employ microwaves [8], [9], [10] and ultrasound [11]. However, these approaches require a significant amount of training data and do not offer quantitative evaluations based on physical properties. In addition, recent studies [12], [13], [14], [15] have identified that complex permittivity is a key parameter for classifying rust types, such as black, salt, and red rust. This suggests that characterizing the dielectric parameters is becoming more vital for advanced NDT techniques [16], [17].

By solving the domain integral equation, inverse scattering (IS) analysis, also known as tomography, can provide quantitative reconstruction in terms of complex permittivity. Because this inverse problem is ill-conditioned and nonlinear, different nonlinear inversion methods, such as linear approximation-based diffraction tomography [18], and distorted Born iterative method (DBIM) [19], [20], [21], have been proposed. Among these approaches, contrast source inversion (CSI) [22] is the most promising solution owing to its low complexity and applicability to real scenarios, and many studies have assumed

Manuscript received 16 April 2023; revised 29 August 2023 and 25 October 2023; accepted 28 October 2023. Date of publication 8 November 2023; date of current version 23 November 2023. This work was supported in part by the JST FOREST Program under Grant JPMJFR2025, and in part by the commissioned research of 'National Institute for Land and Infrastructure Management, under technology research and development system of 'The Committee on Advanced Road Technology' established by MLIT, Japan. *(Corresponding author: Shouhei Kidera.)*

Katsuyoshi Suzuki and Shouhei Kidera are with the Graduate School of Informatics and Engineering, The University of Electro-Communications, Chofu 182-8585, Japan (e-mail: suzuki.katsuyoshi@ems.cei.uec.ac.jp; kidera@uec.ac.jp).

Shingo Nakamura is with the Sensing Technology Research Department, Fuji Electric Company Ltd., Hino-shi 108-0075, Japan (e-mail: nakamura-shin@fujielectric.com).

Digital Object Identifier 10.1109/JSTARS.2023.3331257

nondestructive evaluation or subsurface imaging scenarios [23], [24], [25], [26]. Meanwhile, the CSI or other IS approaches suffer from inaccuracy due to ill-posed conditions [i.e., the number of unknowns allocated to the region of interest (ROI) considerably outnumbers that of measurements (data), especially for the general NDT model] because the illumination angle to object is severely limited. To address the above problem, a sparse regularization algorithm [27], [28] has been developed, but it requires a much expensive computational cost in the optimization process. To address nonlinearity, deep learning (DL) solutions have been developed extensively [29], [30], [31], [32], [33], [34]. These studies have shown that such nonlinear issues can be effectively optimized, even in full-wave 3-D models or experimental setups [35]. However, the accuracy of the DL-based approach is largely dependent on both the pretraining dataset and the DL structure. Moreover, only a few studies have applied the DL NIS approach to NDT models. Such models must contend with highly ill-posed conditions and high-contrast buried objects, such as air or water-filled materials, set against a concrete background. Another solution is the hybrid use of the radar approach: a radar image is used for prior knowledge of the post-IS optimization problem. Our previous study [36] demonstrated that the RPM prior-based CSI offers a distinct advantage from the traditional CSI by limiting the ROI (reducing the number of unknowns), assuming the NDT model. However, the study only demonstrated the effectiveness of a simplified 2-D numerical model.

In light of the foregoing, we present an experimental investigation of real-world road specimens using commercially available S-band ultrawideband radar equipment, the part of which has been introduced in [37]. We believe that quite few studies have explored experimental or real-world data investigations for quantitative reconstruction of realistic road models using a water content cavity model between asphalt and floorboard in microwave NDT applications. In addition, the initial estimate of the permittivity and conductivity of an object is introduced by minimizing the cost function in the CSI. Notably, a similar approach was proposed in literature [38] to avoid a local optimal solution. Furthermore, the relative permittivity can be determined accurately by the maximum response of the radar image focusing on the rebar response, which does not require prior knowledge about the depth of the rebar position or its cover thickness. By introducing an existing efficient calibration procedure [26], [42], we demonstrate that the proposed hybrid approach with RPM and CSI provides more accurate quantitative reconstruction for the dielectric profile of buried objects, e.g., an air cavity or water, located at the boundary between asphalt and concrete floorboards.

Our primary contributions are summarized as follows.

1) Radar $\rightarrow$ Tomography: The RPM-based ROI limitation enhances the post-CSI-based permittivity reconstruction significantly by reducing the number of unknowns drastically.
2) The initial estimate using the CSI cost function is introduced to achieve accurate reconstruction of a high contrast object, e.g., a water-filled cavity in concrete media.
3) We propose an automatic determination process for the relative permittivity of the background (concrete) media that focuses on the rebar pipe and does not require prior knowledge of concrete cover thickness or the depth of the rebar position.
4) The experimental validation, assuming the realistic road model with a thin-layer water-filled cavity demonstrates that the proposed scheme enhances the reconstruction accuracy of permittivity and conductivity considerably, even when using commercial UWB radar equipment.

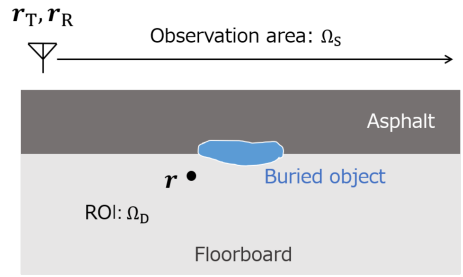

Fig. 1. Observation model, assuming concrete road NDE application.

II. Method

A. Observation Model

Fig. 1 shows the observation geometry, assuming the typical NDT model, in which the background concrete media forms two planar layers with asphalt and floorboard. A set of transmitter and receiver is scanned along the horizontal axis at the observation area, which is defined as Ω_S, that is, monostatic radar model is assumed. The ROI is defined as Ω_D, which usually includes a whole part of the background concrete media in the inversion scheme. $E^T(\omega; \boldsymbol{r}_T, \boldsymbol{r}_R)$ denotes a total electric field observed at position $\boldsymbol{r}_R$, which is illuminated and scattered from the point source transmitter at $\boldsymbol{r}_T$, at a specific angular frequency ω. Here, the scattered electric field $E^S(\omega; \boldsymbol{r}_T, \boldsymbol{r}_R)$ is defined as follows:

$$E^S(\omega; \boldsymbol{r}_T, \boldsymbol{r}_R) \equiv E^T(\omega; \boldsymbol{r}_T, \boldsymbol{r}_R) - E^I(\omega; \boldsymbol{r}_T, \boldsymbol{r}_R). \quad (1)$$

$E^I(\omega; \boldsymbol{r}_T, \boldsymbol{r}_R)$ denotes the incident electric fields, which are usually observed when the object is absent. Notably, the complex permittivity and thickness of each concrete layer are given, for simplicity.

Here, the matched filter output of $E^S(\omega; \boldsymbol{r}_T, \boldsymbol{r}_R)$ is defined as $e(R; \boldsymbol{r}_T, \boldsymbol{r}_R)$, where $R = ct/2$, t is defined as time, and the propagation speed in the air as c. Here, to apply the RPM scheme, the range point $\boldsymbol{q}_i \equiv (\boldsymbol{r}_{T,i}, \boldsymbol{r}_{R,i}, R_i)$ is extracted from the local maxima of $e(t; \boldsymbol{r}_T, \boldsymbol{r}_R)$ to R.

B. Contrast Source Inversion

Here, we briefly introduce the CSI inversion scheme. The domain integral equation expresses the predefined scattered electric field $E^S(\omega; \boldsymbol{r}_T, \boldsymbol{r}_R)$ as

$$E^S(\omega; \boldsymbol{r}_T, \boldsymbol{r}_R) = k_B^2 \int_{\Omega_D} G_B(\omega; \boldsymbol{r}, \boldsymbol{r}_R) \xi(\omega; \boldsymbol{r}_T, \boldsymbol{r}) d\boldsymbol{r} \quad (2)$$

where k_{B} and $G_{\mathrm{B}}(\omega;\boldsymbol{r},\boldsymbol{r}_{\mathrm{R}})$ denote the wave number and the Green's function of the background media, respectively. $\chi(\omega;\boldsymbol{r})\equiv(\epsilon^{\mathrm{c}}(\omega;\boldsymbol{r})-\epsilon^{\mathrm{c}}_{\mathrm{B}}(\boldsymbol{r}))/\epsilon^{\mathrm{c}}_{\mathrm{B}}(\boldsymbol{r})$ denotes the contrast function, where $\epsilon^{\mathrm{c}}(\omega;\boldsymbol{r})$ and $\epsilon^{\mathrm{c}}_{\mathrm{B}}(\boldsymbol{r})$ are complex permittivities at the angular frequency ω and the position $\boldsymbol{r}$ with and without an object, respectively. The dummy variable, as a contrast source, $\xi(\omega;\boldsymbol{r}_{\mathrm{T}},\boldsymbol{r})\equiv\chi(\omega;\boldsymbol{r})E^{\mathrm{T}}(\omega;\boldsymbol{r}_{\mathrm{T}},\boldsymbol{r})$ is introduced. In the CSI optimization scheme, the physical constraints are implemented so that (2) must be satisfied at Ω_{S} and Ω_{D}. To be more specific, the CSI minimizes the following cost function, in terms of $\chi(\omega;\boldsymbol{r})$, $E^{\mathrm{T}}(\omega;\boldsymbol{r}_{\mathrm{T}},\boldsymbol{r})$, and $\xi(\omega;\boldsymbol{r}_{\mathrm{T}},\boldsymbol{r})$ as follows:

$$F(\chi,w)\equiv\frac{\sum_{\boldsymbol{r}_{\mathrm{T}}}\|E^{\mathrm{S}}(\omega;\boldsymbol{r}_{\mathrm{T}},\boldsymbol{r}_{\mathrm{R}})-\mathcal{G}^{S}[w]\|^2_{\Omega_{\mathrm{S}}}}{\sum_{\boldsymbol{r}_{\mathrm{T}}}\|E^{\mathrm{S}}(\omega;\boldsymbol{r}_{\mathrm{T}},\boldsymbol{r}_{\mathrm{R}})\|^2_{\Omega_{\mathrm{S}}}}+\lambda\frac{\sum_{\boldsymbol{r}_{\mathrm{T}}}\|\chi(\boldsymbol{r})E^{\mathrm{I}}(\omega;\boldsymbol{r}_{\mathrm{T}},\boldsymbol{r}')-\xi(\omega;\boldsymbol{r}_{\mathrm{T}},\boldsymbol{r})+\chi(\boldsymbol{r})\mathcal{G}^{D}[w]\|^2_{\Omega_{\mathrm{D}}}}{\sum_{\boldsymbol{r}_{\mathrm{T}}}\|\chi(\omega;\boldsymbol{r})E^{\mathrm{I}}(\omega;\boldsymbol{r}_{\mathrm{T}},\boldsymbol{r}')\|^2_{\Omega_{\mathrm{D}}}} \tag{3}$$

where λ denotes the regularization coefficient, and the operators $\mathcal{G}^{S}$ and $\mathcal{G}^{D}$ are defined as

$$\mathcal{G}^{S}[w]=k_{\mathrm{B}}^2\int_{\Omega_{\mathrm{D}}}G^{B}(\omega;\boldsymbol{r}_{\mathrm{R}},\boldsymbol{r})\xi(\omega;\boldsymbol{r}_{\mathrm{T}},\boldsymbol{r})d\boldsymbol{r},(\boldsymbol{r}_{\mathrm{R}}\in\Omega_{\mathrm{S}}) \tag{4}$$

$$\mathcal{G}^{D}[w]=k_{\mathrm{B}}^2\int_{\Omega_{\mathrm{D}}}G^{B}(\omega;\boldsymbol{r}',\boldsymbol{r})\xi(\omega;\boldsymbol{r}_{\mathrm{T}},\boldsymbol{r})d\boldsymbol{r},(\boldsymbol{r}'\in\Omega_{\mathrm{D}}). \tag{5}$$

$\|\cdot\|^2_{\Omega_{\mathrm{S}}}$ and $\|\cdot\|^2_{\Omega_{\mathrm{D}}}$ denote the l_2 norms calculated in Ω_{S} and Ω_{D}, respectively. As a distinct feature of the CSI, the variable $E^{\mathrm{T}}(\omega;\boldsymbol{r}_{\mathrm{T}},\boldsymbol{r})(\boldsymbol{r}\in\Omega_{\mathrm{D}})$ is optimized with $\xi(\boldsymbol{r}_{\mathrm{T}},\boldsymbol{r})$ and $\chi(\omega;\boldsymbol{r})$; that is, the iterative calculation of $E^{\mathrm{T}}(\omega;\boldsymbol{r}_{\mathrm{T}},\boldsymbol{r})$ using a forward solver, such as FDTD, could be avoided, thereby reducing the computational cost. However, because the unknown cells are allocated to a whole part of the concrete media, the number of these unknowns remarkably exceeds that of the data (measurement points and frequency bins), and such an ill-posed condition worsens in the NDT observation model due to limited observation angles. Thus, the ROI limitation scheme would be a promising solution for the abovementioned problem because the buried object's existing area is usually sparsely distributed within the concrete media, and this scheme significantly reduces the number of unknowns allocated to the ROI.

C. RPM Prior-Based ROI Estimate

The study [36] introduced a radar-based ROI limitation scheme in which an RPM method was introduced in the radar imaging process. The RPM converts each range point $\boldsymbol{q}_i$ to the associated scattering center as $\boldsymbol{q}_i$ to the associated scattering center as $\boldsymbol{p}(\boldsymbol{q}_i)$ via a Gaussian kernel density estimation as follows:

$$\hat{\boldsymbol{p}}(\boldsymbol{q}_i)=\boldsymbol{r}_{\mathrm{c},i}+\begin{bmatrix}\cos\hat{\theta}(\boldsymbol{q}_i)\\ \sin\hat{\theta}(\boldsymbol{q}_i)\end{bmatrix}. \tag{6}$$

Here, $\boldsymbol{r}_{\mathrm{c},i}\equiv\frac{(\boldsymbol{r}_{\mathrm{T},i}+\boldsymbol{r}_{\mathrm{R},i})}{2}$, and $\hat{\theta}(\boldsymbol{q}_i)$ is calculated as

$$\hat{\theta}(\boldsymbol{q}_i)=\arg\max_{\theta}\sum_{j}|s(\boldsymbol{q}_j)| \tag{7}$$

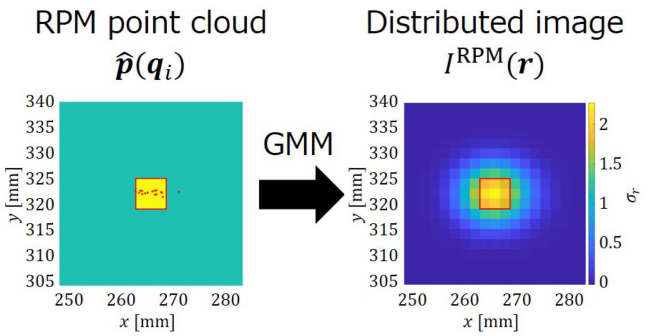

Fig. 2. Conversion from RPM point cloud $\hat{\boldsymbol{p}}(\boldsymbol{q}_i)$ to the distributed image $I^{\mathrm{RPM}}(\boldsymbol{r})$ via GMM.

$$\times\exp\left\{-\frac{|\theta-\theta(\boldsymbol{q}_i,\boldsymbol{q}_j)|^2}{2\sigma_\theta^2}\right\}\exp\left\{-\frac{||\boldsymbol{r}_{\mathrm{c},i}-\boldsymbol{r}_{\mathrm{c},j}||^2}{2\sigma_X^2}\right\} \tag{8}$$

where $\theta(\boldsymbol{q}_i,\boldsymbol{q}_j)$ denotes the angle of arrival from the scattered center to $\boldsymbol{r}_{\mathrm{c},i}$, which is determined by the intersection point of the two circles with the centers as $\boldsymbol{r}_{\mathrm{c},i}$ and $\boldsymbol{r}_{\mathrm{c},j}$ and the radii as R_i and R_j, respectively, under the geometrical optics approximation with a dielectric constant of the background media. In addition, σ_θ and σ_X are constant parameters. These can be determined based on the specific criteria. For instance, σ_θ is determined considering by the spatial profile of the accumulated intersection points, namely, the presumed aperture angle. Meanwhile, σ_X should be aligned with the element intervals. The detail of these sensitivities has been described in [7]. Many studies have validated that the RPM offers a point cloud image that expresses a target boundary, i.e., a scattering center point, even in complicated and multiobject scenarios, which have been discussed in [5], [7].

To obtain the ROI area from the above RPM point cloud image, the group of scattering center points reconstructed by the RPM is converted to the following distributed image as $I^{\mathrm{RPM}}(\boldsymbol{r})$ using a Gaussian mixture model (GMM) as

$$I^{\mathrm{RPM}}(\boldsymbol{r})=\sum_{k=1}^{N}\frac{\pi_k}{\sqrt{(2\pi)^m|\boldsymbol{\Sigma}_k|}}\times\exp\left\{-\frac{1}{2}(\boldsymbol{r}-\boldsymbol{\mu}_k)^{\mathrm{T}}\boldsymbol{\Sigma}^{-1}(\boldsymbol{r}-\boldsymbol{\mu}_k)\right\} \tag{9}$$

where N is the number of clusters. π_k, $\boldsymbol{\mu}_k$, and $\boldsymbol{\Sigma}_k$ denote weights, mean vector, and covariance matrix, respectively, for the kth cluster, which are determined by the group of $\hat{\boldsymbol{p}}^{(k)}(\boldsymbol{q}_i)$. Here, the hyperparameters, such as $\pi_k,\boldsymbol{\mu}_k$, and $\boldsymbol{\Sigma}_k$ can be optimized in the maximum likelihood procedure using the expectation maximization (EM) algorithm [43]. Fig. 2 illustrates the conversion process from the RPM point-cloud to the 2-D distributed image using the GMM model.

Then, the ROI region $I^{\mathrm{RPM}}_{\mathrm{BI}}(\boldsymbol{r})$ is determined as

$$I^{\mathrm{RPM}}_{\mathrm{BI}}(\boldsymbol{r};\alpha)\equiv\begin{cases}1 & (I^{\mathrm{RPM}}(\boldsymbol{r})\geq\alpha\max_{\boldsymbol{r}}I^{\mathrm{RPM}}(\boldsymbol{r}))\\ 0 & (\text{otherwise})\end{cases} \tag{10}$$

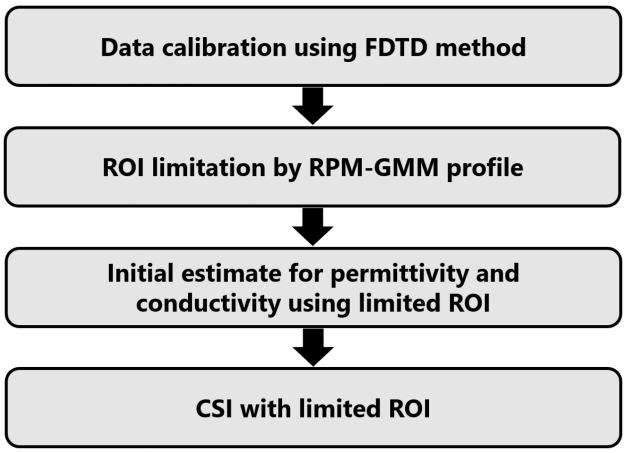

Fig. 3. Processing flow of the proposed method.

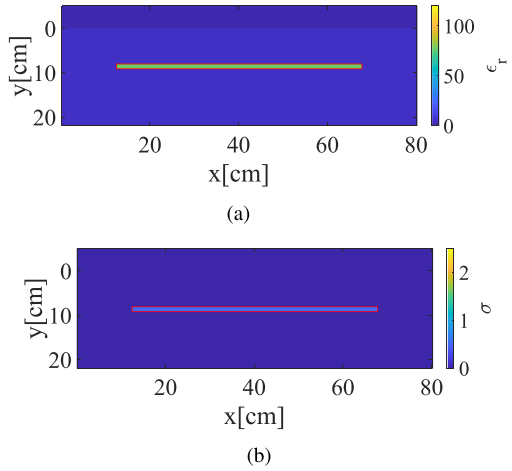

Fig. 4. Original profile of permittivity and conductivity. (a) Permittivity. (b) Conductivity.

where α denotes the threshold parameter. Then, the ROI is redefined as

$$\tilde{\Omega}_{\mathrm{D}} = \left\{ \boldsymbol{r} | I_{\mathrm{BI}}^{\mathrm{RPM}}(\boldsymbol{r}; \alpha) > 0 \right\}. \tag{11}$$

Then, the CSI with a limited ROI denoted as $\tilde{\Omega}(\alpha)$ is carried out to obtain a dielectric profile of the object. The details of the methodology and process are described in [36].

D. Initial Estimate and CSI Optimization

In addition, to provide an appropriate initial estimate of permittivity and conductivity, a global search algorithm with few iterations is introduced to minimize the cost function of CSI in (3). Here, we assume that a buried object has a homogeneous property with constant permittivity and conductivity as $(\epsilon_{\mathrm{obj}}, \sigma_{\mathrm{obj}})$. In other words, each profile is defined as follows:

$$(\epsilon(\boldsymbol{r}; \epsilon_{\mathrm{obj}}), \sigma(\boldsymbol{r}; \sigma_{\mathrm{obj}})) \equiv \begin{cases} (\epsilon_{\mathrm{obj}}, \sigma_{\mathrm{obj}}), & (\boldsymbol{r} \in \tilde{\Omega}_{\mathrm{D}}) \\ (\epsilon_{\mathrm{B}}, \sigma_{\mathrm{B}}), & (\boldsymbol{r} \notin \tilde{\Omega}_{\mathrm{D}}). \end{cases} \tag{12}$$

Under the above assumption, the complex permittivity is defined as $\tilde{\epsilon}^{\mathrm{c}}(\omega, \boldsymbol{r}; \epsilon_{\mathrm{obj}}, \sigma_{\mathrm{obj}}) \equiv \epsilon(\boldsymbol{r}; \epsilon_{\mathrm{obj}}) - \dfrac{j\sigma(\boldsymbol{r}; \sigma_{\mathrm{obj}})}{\omega \epsilon_0}$. Then, the contrast function is defined as $\tilde{\chi}(\omega, \boldsymbol{r}; \epsilon_{\mathrm{obj}}, \sigma_{\mathrm{obj}}) \equiv (\tilde{\epsilon}^{\mathrm{c}}(\omega; \boldsymbol{r}; \epsilon_{\mathrm{obj}}, \sigma_{\mathrm{obj}}) - \epsilon_{\mathrm{B}}^{\mathrm{c}}(\boldsymbol{r}))/\epsilon_{\mathrm{B}}^{\mathrm{c}}(\boldsymbol{r})$.

Thus, the combination of $\epsilon_{\mathrm{obj}}^{\mathrm{re}}$ and σ_{obj} are optimized as follows:

$$(\hat{\epsilon}_{\mathrm{obj}}, \hat{\sigma}_{\mathrm{obj}}) = \underset{(\epsilon_{\mathrm{obj}}, \sigma_{\mathrm{obj}})}{\arg\min}\, F(\tilde{\chi}(\omega, \boldsymbol{r}; \epsilon_{\mathrm{obj}}, \sigma_{\mathrm{obj}}), w). \tag{13}$$

In the CSI optimization sequences, the total field $E^{\mathrm{T}}(\omega; \boldsymbol{r}_{\mathrm{T}}, \boldsymbol{r})$ and contrast source w are optimized when calculating $F(\chi_{\mathrm{obj}}, w)$, where the contrast function is fixed as χ_{obj}. This scheme can reduce the number of unknowns, and yield much faster convergence of the optimization, if we assume an appropriate combination of $\epsilon_{\mathrm{obj}}^{\mathrm{re}}$ and σ_{obj}. Finally, the above contrast function as $\hat{\chi}_{\mathrm{obj}}(\omega)$ is used for the initial estimate of the post-CSI process, where both χ and w are updated in the optimization process. Fig. 3 shows the processing flow of this method. The proposed scheme is expected to enhance a reconstruction accuracy due to the reduced number of unknowns and a more appropriate initial estimate.

TABLE I
DIELECTRIC PROPERTIES AND SIZE OF BACKGROUND MEDIUM AND EACH TARGET

	ϵ_r	σ [S/m]	size [mm]
Background medium	5.1	0.001	800 × 220
Water	77.0	0.537	550 × 12

III. Results in Numerical Test

A. Numerical Setup

At first, the 2-D FDTD numerical test, assuming the typical NDT model, is presented as follows. We assume the bistatic observation model, where a set of transmitter and receiver with 60-mm separation as D_{bi} is scanned along x-axis. The observation data is acquired with 10-mm interval with this bistatic radar at the line 20 mm far from the concrete surface. The transmitted current forms the Gaussian modulated pulse with the center frequency of 2.45 GHz and the effective bandwidth of 2.70 GHz. A point source and sensor are assumed at transmitter and receiver. Fig. 4 shows the original profile of the background media and water-filled object for relative permittivity and conductivity. The dimensions and dielectric properties of each object and background media are summarized in Table I. In this simulation, the dimension and dielectric property of the background concrete media is given, and the rebar object buried into concrete material is not considered, to assess the reconstruction performance of dielectric profile under the ideal situation. Here, we assume the single-layered homogeneous concrete media as background media, which has nondispersive dielectric feature in this frequency band, demonstrated in some literature [12]. The cell size for FDTD and CSI inversion is set to 2-mm square. We assume a water-filled material located at the inner area of concrete material with 80-mm below from the surface, which models an anomaly area between asphalt and concrete floor board, as shown in Fig. 1.

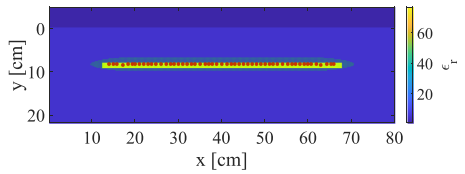

Fig. 5. Reconstruction of RPM point cloud and the extracted ROI by the RPM GMM model. Red dots are the RPM image. Green dots are the extracted ROI cells. Color denotes the relative permittivity.

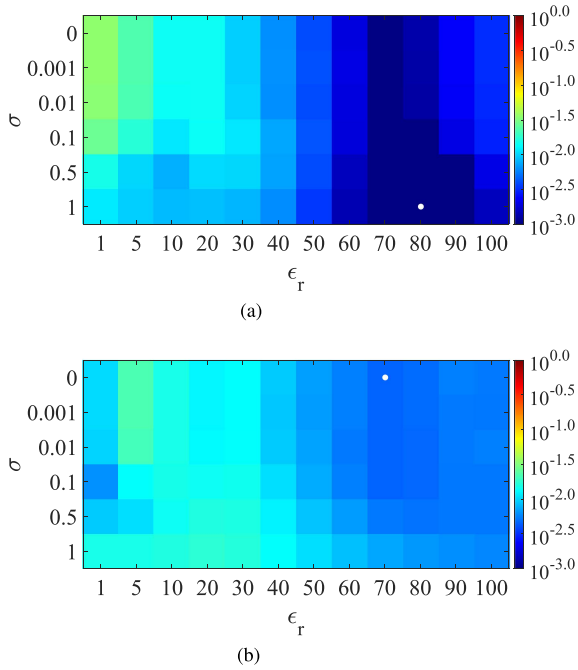

Fig. 6. Distribution of residual of the CSI cost function in each case using FDTD data. White dot denotes the minimal solution. Color denotes the residual of the cost function. (a) True ROI. (b) RPM ROI.

Here, the Green's function of the concrete background media is also given by the FDTD at the absence of buried object. The total number of unknowns, corresponding to a whole area of concrete (background) media, is 44 000.

B. Reconstruction Results

1) RPM-Based ROI Estimate: At first, the RPM-based ROI reconstruction performance is validated as follows, described in Section II-C. Fig. 5 shows the reconstructed RPM imaging points, and the converted distributed image by the GMM as $I^{\mathrm{RPM}}(\boldsymbol{r})$, where each RPM parameter is set as $\sigma_X = 5.0$ mm and $\sigma_\theta = 0.1$ radian. This figure shows the RPM point cloud accurately reconstructs the upper boundary of the buried object, and the GMM distributed area sufficiently covers the actual ROI area. In addition, the selected ROI $I_{\mathrm{BI}}^{\mathrm{RPM}}(\boldsymbol{r};\alpha)$ contains a whole of target region, where the parameter $\alpha = 0.05$ is empirically determined.

2) Initial Estimate of Dielectric Property: Next, the initial value estimation results described in Section II-D, are described as follows. Fig. 6 shows the distributions of the residual values of the minimized cost function as a combination of the relative permittivity and conductivity for the cases using the true ROI and RPM-based ROI (illustrated in Fig. 5). In CSI processing, six frequency points 1.06, 1.15, 1.29, 1.38, 1.47, and 1.56 GHz are used in optimizing the cost function, and the iteration number in fixed contrast function χ_{obj} is 1000. As shown in Fig. 6, for the true ROI, the optimized combination of relative permittivity and conductivity is represented as $(\hat{\epsilon}_{\mathrm{obj}}, \hat{\sigma}_{\mathrm{obj}}) = (80, 1.0\ \mathrm{S/m})$. In contrast, the actual dielectric parameters are defined as $(77, 0.53\ \mathrm{S/m})$. Although the conductivity showed noticeable discrepancies, the relative permittivity was estimated precisely. By narrowing down the ROI and assessing the CSI cost functions, we can provide a suitable starting point for estimates, particularly concerning relative permittivity. Focusing on the case of the RPM-based ROI, the optimized combination has some errors, especially for conductivity direction, and then, it indicates that the ROI accuracy directly affects the initial estimate for the permittivity and conductivity, which has been also demonstrated in [36].

3) Final Reconstruction: Figs. 7 and 8 show the final reconstruction results for the relative permittivity and conductivity, respectively, using the initial estimate with the true and RPM-based ROI, where the iteration number of the post CSI is set to 1000. Focusing on the original CSI approach, namely, without limiting the ROI, it could not provide an actual dielectric property in particular for relative permittivity, because without limiting the ROI, the number of unknowns increases to 44 000, leading to a severely ill-posed condition. On the contrary, the proposed scheme with ROI limitation offers a certain level of reconstruction accuracy especially in using the true ROI, because the preinitial estimate offers more effective convergences and the massively reduced unknowns also contribute to the accuracy enhancement. Note that, the final reconstruction results largely depend on the initial estimate for both permittivity and conductivity, especially for the true ROI cases. For the case in the RPM-based ROI, the final reconstruction are updated especially for the center of ROI in relative permittivity, which corresponds to the true ROI area. Fig. 9 illustrates the residual of the cost function as a function of the number of iterations for each method. The results highlight that our proposed method, particularly when using the true ROI, significantly improved the convergence speed. This improvement is achieved by limiting the ROI, which considerably mitigates ill-posed conditions.

Here, some quantitative metric for accuracy evaluations are introduced. Table II summarizes the error evaluations, where the root mean square errors (RMSE) are used to evaluate relative permittivity and conductivity. The RMSEs for relative permittivity

TABLE II
RMSE FOR RELATIVE PERMITTIVITY AND CONDUCTIVITY IN THE NUMERICAL TEST

	Number of unknowns	$\mathrm{RMSE}_{\epsilon_r}$	RMSE_{σ} [S/m]
CSI w/o ROI limit.	44000	76.0	0.48
CSI w/ ROI limit. (True ROI)	1656	6.0	0.59
CSI w/ ROI limit. (RPM ROI)	4428	15.9	0.50

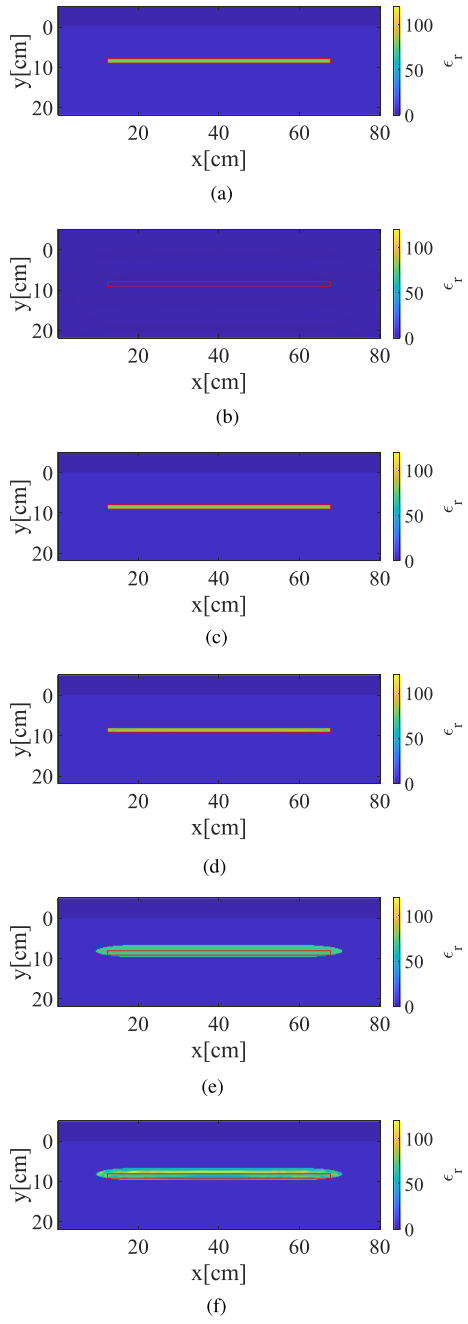

Fig. 7. Reconstruction results of relative permittivity. Color denotes the relative permittivity. Red solid rectangular is the boundary of water-filled object area. (a) Ground truth. (b) CSI w/o ROI limit. (c) Initial estimate w/ROI limit. (True ROI). (d) CSI w/ROI limit. (True ROI). (e) Initial estimate w/ROI limit. (RPM ROI). (f) CSI w/ROI limit. (RPM ROI).

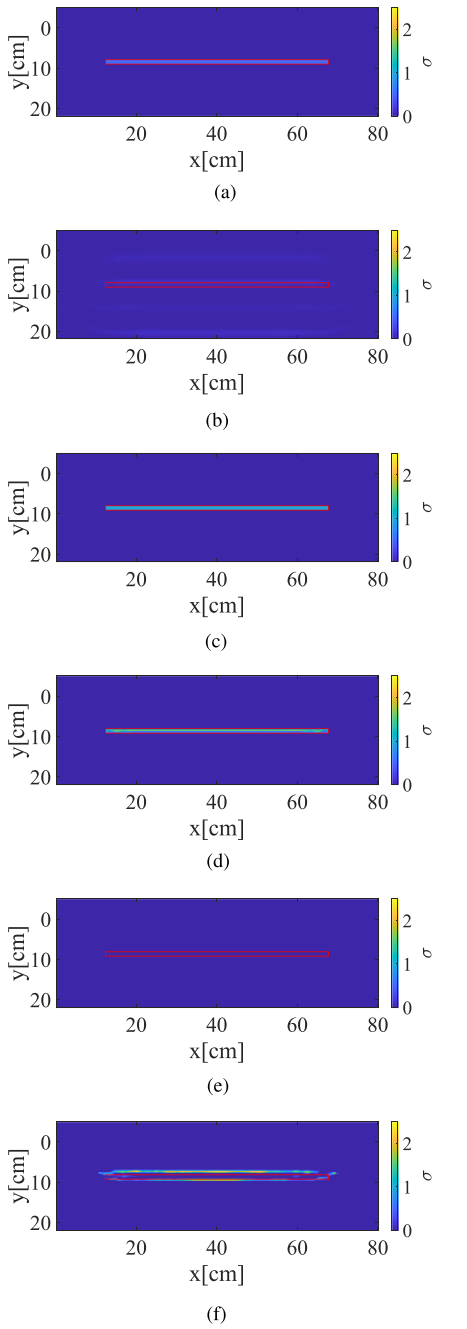

Fig. 8. Reconstruction results of conductivity. Color denotes the relative permittivity. Red solid rectangular is the boundary of water-filled object area. (a) Ground truth. (b) CSI w/o ROI limit. (c) Initial estimate w/ROI limit. (True ROI). (d) CSI w/ROI limit. (True ROI). (e) Initial estimate w/ROI limit. (RPM ROI). (f) CSI w/ROI limit. (RPM ROI).

RMSE_ϵ and conductivity RMSE_σ are defined as follows:

$$\mathrm{RMSE}_\epsilon = \sqrt{\frac{1}{N}\sum_{i=1}^{N} \left|\epsilon^{\mathrm{true}}(\boldsymbol{r}_i) - \epsilon^{\mathrm{est}}(\boldsymbol{r}_i)\right|^2} \tag{14}$$

$$\mathrm{RMSE}_\sigma = \sqrt{\frac{1}{N}\sum_{i=1}^{N} \left|\sigma^{\mathrm{true}}(\boldsymbol{r}_i) - \sigma^{\mathrm{est}}(\boldsymbol{r}_i)\right|^2}. \tag{15}$$

where $\epsilon^{\mathrm{true}}(\boldsymbol{r}_i)$ and $\epsilon^{\mathrm{est}}(\boldsymbol{r}_i)$ denote the true and reconstructed relative permittivities at the location $\boldsymbol{r}_i$, respectively. $\sigma^{\mathrm{true}}(\boldsymbol{r}_i)$ and $\sigma^{\mathrm{est}}(\boldsymbol{r}_i)$ also express the conductivity, defined in the same way as relative permittivity. N denotes the total number of inversion cells allocated to each area. Here, this area is set to only the true ROI for fair comparison. The evaluations show that our proposed method significantly reduces the RMSEs for the relative permittivity, by reducing the number of unknowns and offering suitable initial estimates. However, there are no marked improvement in the reconstruction of the conductivity. The primary reason for this outcome is that while a relative

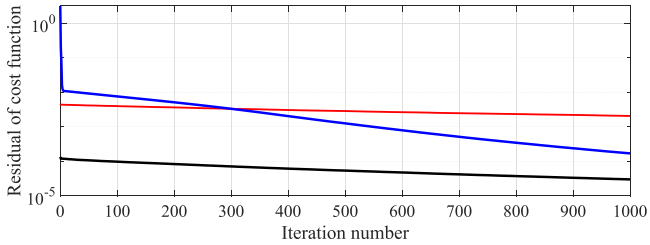

Fig. 9. Residual of the cost function in the CSI in each approach. Blue curve: CSI w/o ROI limit. Black curve: CSI w/ROI limit. (True ROI) Red curve: CSI w/ROI limit. (RPM ROI) .

TABLE III
COMPUTATIONAL TIME REQUIRED FOR SINGLE ITERATION IN EACH METHOD

CSI w/o ROI limit.	CSI w/ ROI limit. (True ROI)	CSI w/ ROI limit. (RPM based ROI)
352.0 s	2.1 s	9.9 s

permittivity is dependent on both phase and magnitude difference of scattered signal, while the conductivity is that while relative permittivity relies on both the phase and magnitude differences of the scattered signal, conductivity is primarily influenced by its magnitude. Given the assumption of a high dielectric contrast object in terms of both permittivity and conductivity, such as a water-filled area set against a low-loss concrete background, we observe minimal variation in the cost functions of (3) for the changes in conductivity compared to those of the relative permittivity, as illustrated in Fig. 6. This insensitivity in the cost function makes it challenging to determine the conductivity with adequate accuracy. However, considering real-world scenarios, we can determine an object's material by assessing only its relative permittivity, which varies significantly between air (1), concrete material (5–10), and water (50–80).

We investigated the computational cost as follows: Table III provides the computational runtime required for a single iteration in each CSI method when using the two Intel Xeon Gold 6330 processors with 2048 GB RAM. Because the original CSI method without an ROI constraint addresses a significantly larger number of unknowns (44 000), its calculation time is much longer than that of the proposed method, which significantly reduces the number of unknowns. In essence, our proposed method with ROI limitation not only improves the reconstruction accuracy but also significantly reduces the computational time required in the inversion process.

4) Sensitivity to Parameters and Additive Noise: This section discusses the sensitivity of reconstruction accuracy when influenced by varying parameters or additive noise. Initially, we address the threshold parameter α, which is used to define the ROI area from the radar image using (10). While we set this parameter to $\alpha = 0.05$ in Section III-B-3), it is anticipated that a larger α would result in a smaller determined ROI and vice versa. Consequently, the parameter α has a direct impact on the reconstruction accuracy of the proposed method, which is evident not only in Fig. 6 but also in Figs. 7 and 8. To highlight the sensitivity of parameter α, we studied two scenarios, where $\alpha = 0.025$ and $\alpha = 0.1$, given that $\alpha = 0.05$, as established in

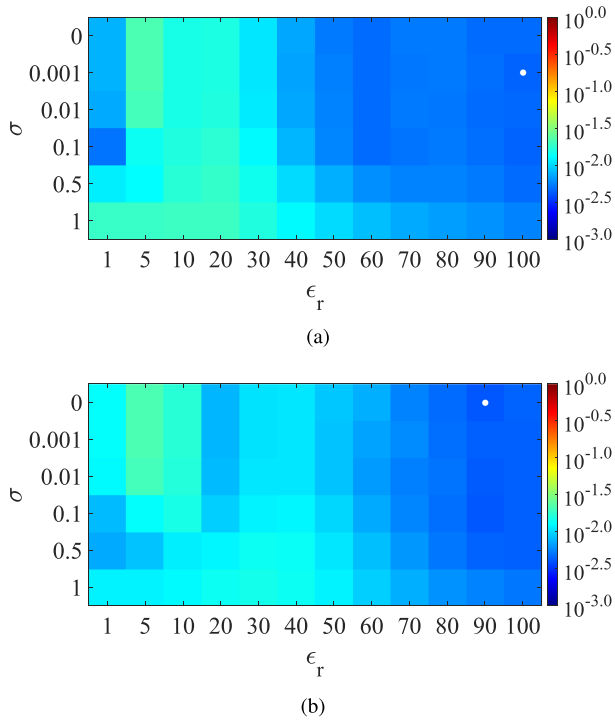

Fig. 10. Distribution of residual of the CSI cost function in changing the parameter α. White dot denotes the minimal solution. Color denotes the residual of the cost function. (a) RPM ROI, $\alpha = 0.025$. (b) RPM ROI, $\alpha = 0.1$.

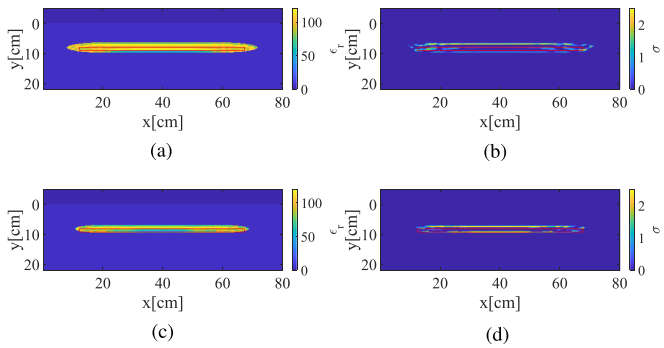

Fig. 11. Reconstruction results of the proposed method with ROI limit (RPM ROI) in changing the parameter α. Color denotes the relative permittivity. 1st column: Relative permittivity. 2nd column: Conductivity. Red solid rectangular is the boundary of water-filled object area. (a) $\alpha = 0.025$. (b) $\alpha = 0.025$. (c) $\alpha = 0.1$. (d) $\alpha = 0.1$.

the results of Section III-B-3). Fig. 10 shows the distribution of the residual of the CSI cost function when $\alpha = 0.025$ and $\alpha = 0.1$. This indicates noticeable differences from the case in which $\alpha = 0.05$, signifying significant sensitivity in relation to the optimal pairing of $(\hat{\epsilon}_{\mathrm{obj}}, \hat{\sigma}_{\mathrm{obj}})$. Fig. 11 illustrates the reconstruction results obtained using the proposed method for $\alpha = 0.025$ and $\alpha = 0.1$ in terms of relative permittivity and conductivity, respectively. Table IV presents the RMSEs for both relative permittivity and conductivity for different values of α. These results underscore the significant influence of α selection on the reconstruction profile. This is attributed to the fact that the extracted ROI area directly sets the number of unknowns. In particular, when dealing with high-contrast objects, such as

TABLE IV
RMSE FOR RELATIVE PERMITTIVITY AND CONDUCTIVITY IN CHANGING THE PARAMETER α

	Number of unknowns	$\mathrm{RMSE}_{\epsilon_r}$	RMSE_{σ} [S/m]
$\alpha = 0.025$	4949	26.81	0.50
$\alpha = 0.05$	4428	15.9	0.50
$\alpha = 0.1$	3533	17.44	0.79

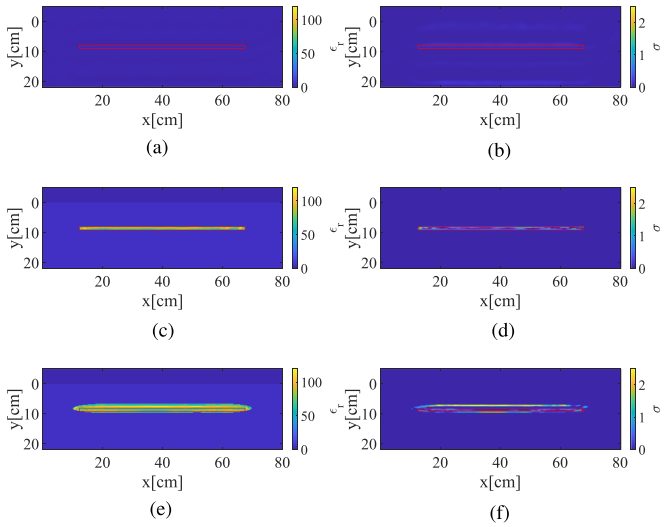

Fig. 12. Reconstruction results of relative permittivity and conductivity at the case of 20-dB SNR. 1st column: Relative permittivity. 2nd column: Conductivity. Color denotes the relative permittivity. Red solid rectangular is the boundary of water-filled object area. (a) CSI w/o ROI limit. (b) CSI w/o ROI limit. (c) CSI w/ROI limit. (True ROI) (d) CSI w/ROI limit. (True ROI). (e) CSI w/ROI limit. (RPM ROI). (f) CSI w/ROI limit. (RPM ROI).

water, these ROI selections profoundly impact reconstruction accuracy. However, using our proposed method, we can consistently achieve a much higher relative permittivity for any given α, a feature that is challenging without employing the ROI limitation scheme. Various techniques have been developed to optimize the threshold parameter α based on distributed radar images. Examples include the Otsu's discriminant analysis and its derivative methods [39], [40], [41]. Another notable solution is our distinct approach of updating the ROI using the cost function of the CSI [36]. Integrating these techniques will be the key focus of our future work.

Next, we examined the sensitivity of each method to additive noise. White Gaussian noise was introduced to the received signal in the time domain. The signal-to-noise ratio (SNR) is defined as the ratio of the maximum signal power to the noise power, that is, the variance of the Gaussian distribution. It is worth noting that the signal incorporates a reflection response from the buried object, but excludes surface reflection from the upper surface of the concrete medium. Our investigation focused on an SNR level of 20 dB. Fig. 12 displays the reconstruction results for each method with respect to relative permittivity and conductivity. Table V lists the RMSEs for the relative permittivity and conductivity in this context. These findings suggest that there is no significant sensitivity to random noise at this SNR level. This stability can be attributed to the use of multiple

TABLE V
RMSE FOR RELATIVE PERMITTIVITY AND CONDUCTIVITY IN THE NUMERICAL TEST AT 20 DB SNR

	Number of unknowns	$\mathrm{RMSE}_{\epsilon_r}$	RMSE_{σ} [S/m]
CSI w/o ROI limit.	44000	75.41	0.48
CSI w/ ROI limit. (True ROI)	1656	7.95	0.33
CSI w/ ROI limit. (RPM ROI)	4125	7.71	0.46

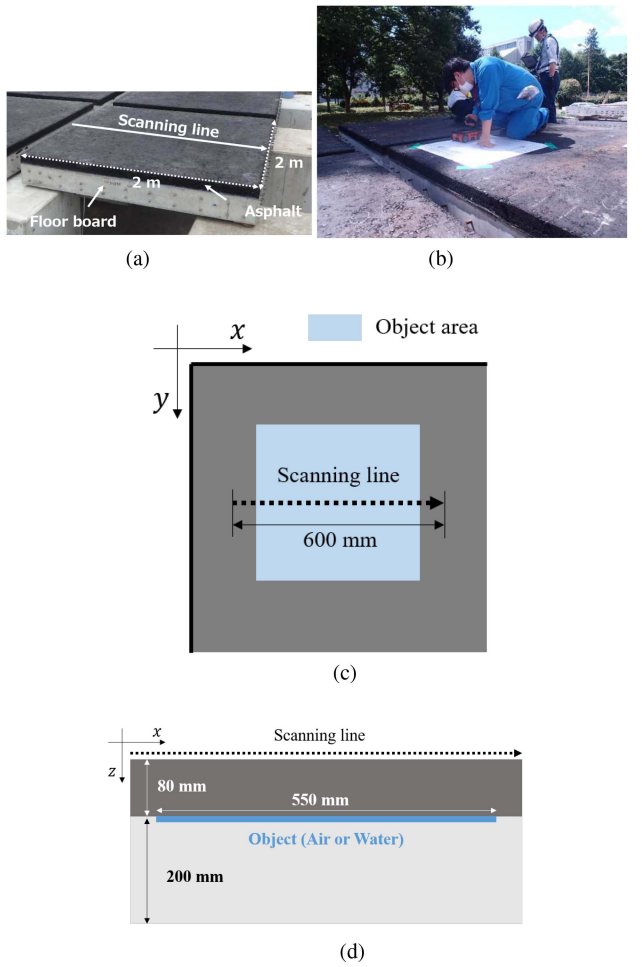

Fig. 13. Experimental scene and observation geometry. (a) Sample under test. (b) Measurement scene. (c) Geometry (X-Y). (d) Geometry (X-Z).

frequency samples (specifically, six samples) to determine the initial estimate for the combination of $(\hat{\epsilon}_{\mathrm{obj}}, \hat{\sigma}_{\mathrm{obj}})$. Moreover, the RPM image is recognized as a noise-resistant radar imaging algorithm that leverages the global profile of the obtained range points [7].

IV. RESULTS IN EXPERIMENTAL TEST

A. Experimental Setup

Fig. 13 shows the experimental site and target model, assuming an actual NDT inspection, and focusing on the detection of air crack or water leakage at the area between asphalt and floorboard. The commercial UWB radar module, Structure Scan

SIR-EZXT by GSSI Inc., is used, which has a center frequency of 2.7 GHz and a bandwidth of 2.7 GHz. In this module, a half wavelength dipole antenna is used as a transmitter and receiver, whose separation is 60 mm. This radar module is scanned along the x-axis with a 600-mm aperture length and 2.5-mm spacing: 241 measurement points are used for imaging analysis. Here, we assume that both asphalt and floorboard have the same relative permittivity (5.1) and conductivity (0.001 S/m), for simplicity. The object area forms 550 × 550 mm dimension with 10-mm thickness, which is located at the upper surface of the floorboard. We assume a water-filled cavity same as in the numerical test, where the water has a relative permittivity of 77.0 and conductivity of 0.537 S/m.

B. Calibration Procedure

This section describes the calibration procedure that transforms the experimental data into the corresponding simulation data. This was achieved using a linear transfer function model, as discussed in [35], [42], [44], [45]. Initially, we measured the reflection responses assuming that the ROI contained only air (serving as the calibration object). These responses were also produced by the FDTD simulation. Let $E^{\mathrm{T}}_{\mathrm{sim}}(\omega)$ and $E^{\mathrm{I}}_{\mathrm{sim}}(\omega)$ be the total and incident electric fields generated by the FDTD method at a specific transmitter and receiver pair, respectively, assuming the calibration object. Meanwhile, $S^{\mathrm{T}}_{\mathrm{exp}}(\omega)$ and $S^{\mathrm{I}}_{\mathrm{exp}}(\omega)$ are the S_{21} parameters in the experiment conducted with and without the calibration objects, respectively. From these, the calibration coefficient $\zeta(\omega)$ is defined as

$$\zeta(\omega) \equiv \frac{E^{\mathrm{T}}_{\mathrm{sim}}(\omega) - E^{\mathrm{I}}_{\mathrm{sim}}(\omega)}{S^{\mathrm{T}}_{\mathrm{exp}}(\omega) - S^{\mathrm{I}}_{\mathrm{exp}}(\omega)}. \tag{16}$$

Utilizing the coefficient $\zeta(\omega)$, the experimental scattered data, represented as $\tilde{S}^{\mathrm{S}}_{\mathrm{exp}}(\omega) \equiv \tilde{S}^{\mathrm{T}}_{\mathrm{exp}}(\omega) - \tilde{S}^{\mathrm{I}}_{\mathrm{exp}}(\omega)$, can be transformed into simulation data, denoted as $\tilde{E}^{\mathrm{S}}_{\mathrm{exp}}(\omega) = \zeta(\omega)\tilde{S}^{\mathrm{S}}_{\mathrm{exp}}(\omega)$. This simulation data are subsequently employed in post-RPM and CSI processing.

C. Reconstruction Results

1) Relative Permittivity Estimate of Background Media: A number of studies demonstrated that the accuracy of the radar image, including the RPM, or the quantitative image using the inverse scattering approach, like CSI, highly depends on the dielectric parameter (relative permittivity) of the background media, namely, the concrete media. In the experiment, it is usually difficult to determine the parameter of relative permittivity under the condition that both thickness and permittivity are unknown, however, we need to estimate this parameter even in this situation, in assuming the real scenario. In this article, we introduce a simple approach to determine the relative permittivity from the traditional radar image, namely, the SAR method. In this case, we use the well-known SAR algorithm, as delay-and-sum (DAS). In the DAS processing, the propagation speed should be given as $v_{\mathrm{bg}} = c_{\mathrm{air}}/\sqrt{\epsilon_{\mathrm{B}}}$, where ϵ_{B} denotes the relative permittivity of background media. Then, we define the DAS image as a function of ϵ_{B}, as $I_{\mathrm{DAS}}(\boldsymbol{r}; \epsilon_{\mathrm{B}})$. In the realistic case, there are rebar pipes buried into the concrete floorboard, and their responses from the rebar forms a hyperbolic curve, because the rebar shape should be regarded as point target in the 2-D model approximation. In this assumption, the optimal relative permittivity of the background media is determined as follows:

$$\hat{\epsilon_{\mathrm{B}}} = \arg\max_{\epsilon_{\mathrm{B}}} \|I_{\mathrm{SAR}}(\boldsymbol{r}; \epsilon_{\mathrm{B}})\|. \tag{17}$$

This approach has a notable feature that it does need a prior knowledge of the depth of the rebar position or thickness of asphalt or concrete floorboard, but only assumes that if we set an appropriate relative permittivity of background, the energy distributed to hyperbolic curve should be focused on the assumed rebar position, and takes a maximum value under energy conservation law. Fig. 14 shows each DAS image assuming different relative permittivity from $\epsilon_{\mathrm{B}} = 4.0$ to $\epsilon_{\mathrm{B}} = 7.0$, the range of which is referred from some literature [47], corresponding to dry and wet concrete state. As shown in Fig. 14, the DAS image mostly focused on the rebar point, in the case of $\epsilon_{\mathrm{B}} = 5.0$ or 5.5. Fig. 15 shows the maximum values of the DAS image as a function of ϵ_{B}, and indicated that the optimal parameter of the ϵ_{B} should be set to 5.1, in this case.

2) RPM-Based ROI Estimate: Fig. 16 shows the distributed radar image determined by the RPM point cloud as $I^{\mathrm{RPM}}(\boldsymbol{r})$ in (9) and the ROI limitation results in (10). In the RPM processing $\sigma_\theta = 0.1$ radian and $\sigma_X = 5$ mm are set, and the parameter $\alpha = 0.05$ in this case. This figure shows that the limited ROI by the RPM accurately covers the actual target shape. In this case, the numbers of unknowns are 44 000 without ROI limitation and 4428 with ROI limitation by the proposed method, and the proposed ROI limitation scheme considerably reduces the number of unknowns less than 10%, which is expected to enhance reconstruction accuracy during post-CSI processing.

3) Initial Estimate of Dielectric Property: Next, we show the results in the initial estimate for permittivity and conductivity. Here, to remove the rebar responses from the B-scan data, the transfer function-based clutter suppression method has been introduced. Fig. 17 shows the minimized residual of the CSI cost function in 1000 iteration with the fixed contrast function χ, in the case of the true and RPM-based ROI. In CSI processing, the frequency points and the iteration number are same in the numerical test, as described in Section III. As shown in these results, the initial estimates using the true and RPM ROI offers a high relative permittivity, which are expected to more than 70. In the true ROI case, the optimized combination is $\hat{\epsilon}, \hat{\sigma} = (100, 0.01\ \mathrm{S/m})$, while the RPM ROI case provides the estimation as $\hat{\epsilon}, \hat{\sigma} = (80, 0.1\ \mathrm{S/m})$. Note that, the minimal residual of the cost function in the true ROI is slightly larger than that of the RPM-based ROI, and the conductivity values are relatively lower than that of the water (usually higher than 0.5 S/m). It is considered that the actual water object includes some air void at the upper surface of the ROI, and it causes the lower conductivity estimation. We would also note that there should be calibration error in converting the experimental data to the FDTD data due to using the linear transfer function model

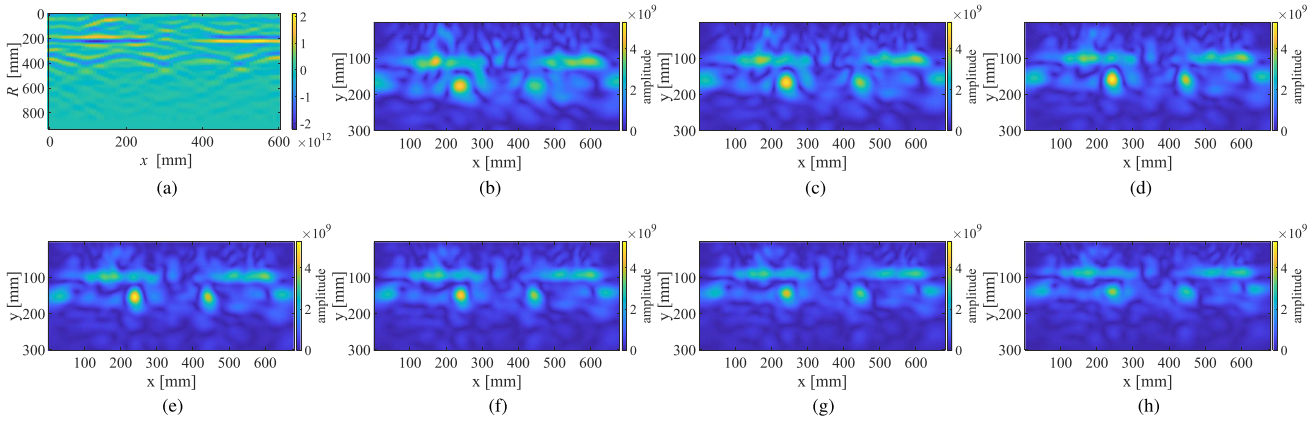

Fig. 14. SAR images $\|I_{\mathrm{SAR}}(\boldsymbol{r};\epsilon_{\mathrm{B}})\|$ using different background permittivities as ϵ_{B}. (a) B-SCAN. (b) $\epsilon_{\mathrm{B}} = 4.0$. (c) $\epsilon_{\mathrm{B}} = 4.5$. (d) $\epsilon_{\mathrm{B}} = 5.0$. (e) $\epsilon_{\mathrm{B}} = 5.5$. (f) $\epsilon_{\mathrm{B}} = 6.0$. (g) $\epsilon_{\mathrm{B}} = 6.5$. (h) $\epsilon_{\mathrm{B}} = 7.0$.

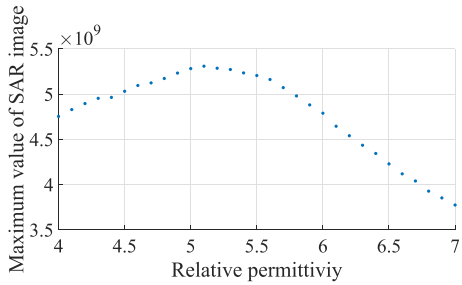

Fig. 15. Maximum values of SAR image as a function of relative permittivity in the experiment. Color denotes the strength of the image.

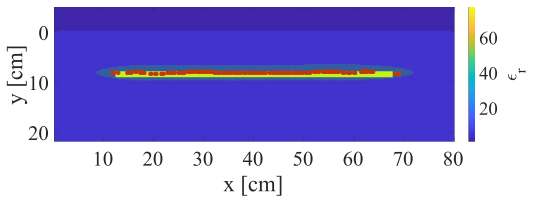

Fig. 16. Extracted ROI by the RPM GMM model in the experiment. Red dots are the RPM image. Green dots are the extracted ROI cells. Color denotes the relative permittivity.

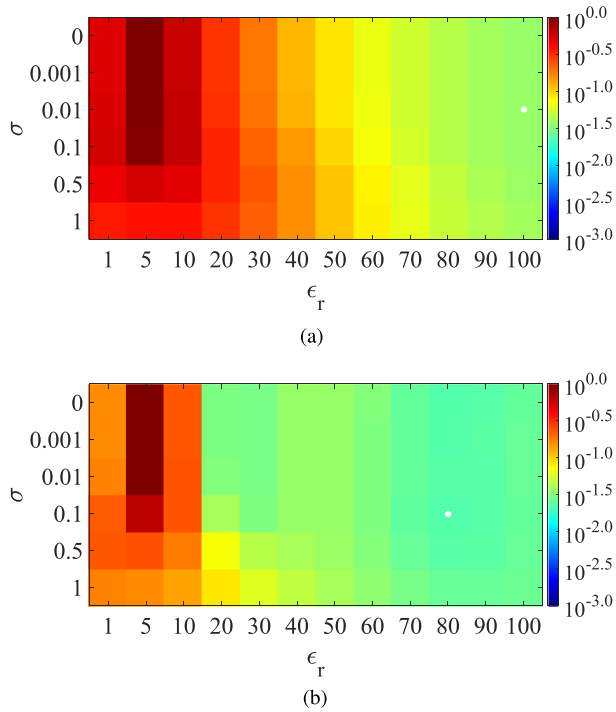

Fig. 17. Distribution of residual of the CSI cost function in each case using the experimental data. White dot denotes the minimal solution. Color denotes the residual of the cost function. (a) True ROI. (b) RPM ROI.

or other clutter components, such as residual response of rebar pipes.

4) Final Reconstruction: Figs. 18 and 19 show the reconstruction results in this case, of relative permittivity and conductivity, respectively. The CSI results obtained without ROI limitation, with 44 000 unknowns, reveal no significant profiles in either case. While the reconstruction around the true ROI is almost identical to dielectric parameters of the background concrete media, we can see some divergence of the estimation outside of the ROI. It implies that the updating process in the original CSI does not work and the solution would diverge due to the severe ill-posed condition and some calibration errors. In contrast, for the CSI with ROI limitation, the results reveal more accurate reconstruction for dielectric profiles in each case. Note that, the cases with the RPM-based ROI [Fig. 18(c) and (d) or Fig. 19(c) and (d)] retain more accurate reconstruction than those with the true ROI, implying that further enhancement of ROI accuracy is promising to obtain more accurate reconstruction of complex permittivity. These results are unexpected. However, one possible explanation is that the actual object area did not align precisely with the true ROI assumed in this case. Achieving a completely flat thin area between the asphalt and floorboard with a uniform thickness is challenging. This suggests that the true ROI may not exactly match with what is illustrated in Figs. 18 or 19. Furthermore, as previously mentioned, the object should have a small air void around the upper surface of the water cavity. This aspect might not have been accounted for in the FDTD-based simulation model. In addition, there could be errors

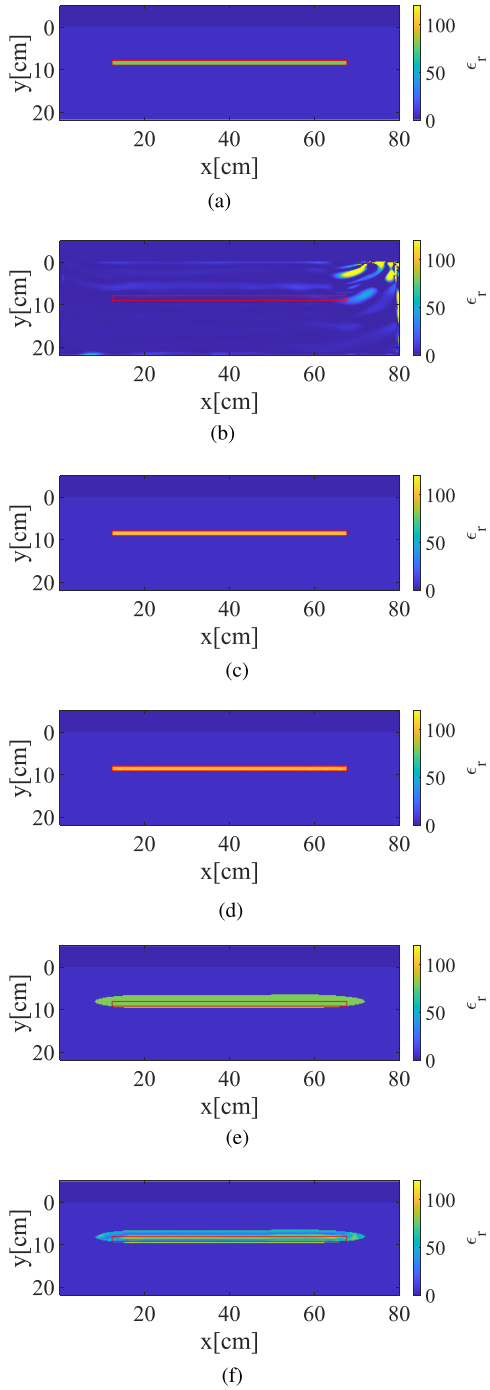

Fig. 18. Reconstruction results of the relative permittivity in the experiment. Color denotes the relative permittivity. Red solid rectangular is the boundary of water-filled object area. (a) Ground truth. (b) CSI w/o ROI limit. (c) Initial estimate w/ROI limit. (True ROI). (d) CSI w/ROI limit. (True ROI). (e) Initial estimate w/ROI limit. (RPM ROI). (f) CSI w/ROI limit. (RPM ROI).

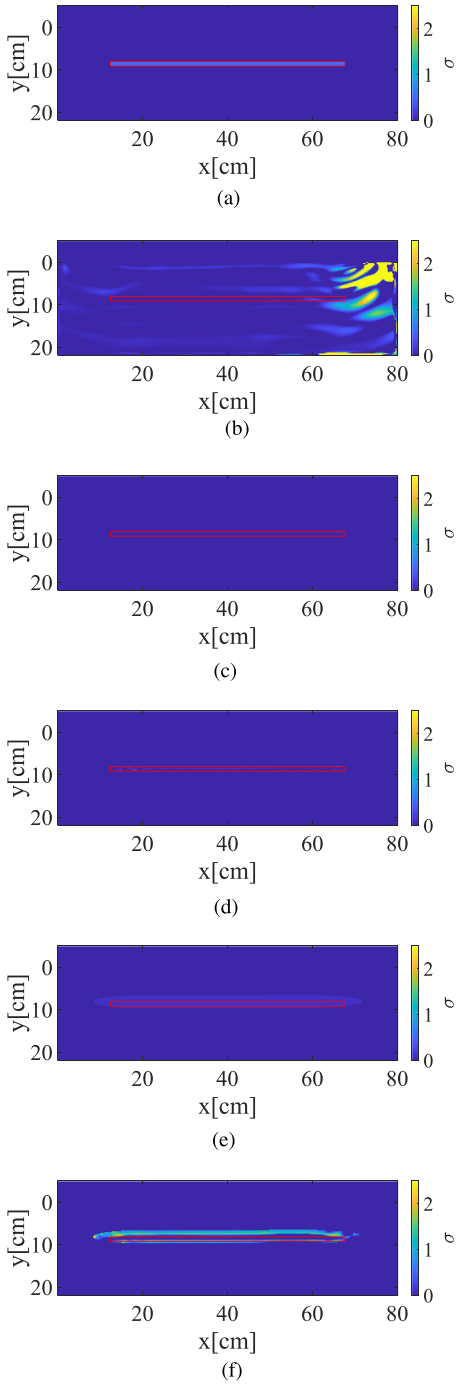

Fig. 19. Reconstruction results of the conductivity in the experiment. Color denotes the relative permittivity. Red solid rectangular is the boundary of water-filled object area. (a) Ground truth. (b) CSI w/o ROI limit. (c) Initial estimate w/ROI limit. (True ROI). (d) CSI w/ROI limit. (True ROI). (e) Initial estimate w/ROI limit. (RPM ROI). (f) CSI w/ROI limit. (RPM ROI).

in the calibration process when converting the experimental data to simulation data.

Finally, Table VI summarizes the RMSE for relative permittivity and conductivity in each case, where each RMSE is calculated only the true ROI area for fair comparison. The table demonstrates that our proposed scheme can provide a more accurate reconstruction of the relative permittivity compared

TABLE VI
RMSE FOR RELATIVE PERMITTIVITY AND CONDUCTIVITY IN THE EXPERIMENT

	Number of unknowns	$\mathrm{RMSE}_{\epsilon_r}$	RMSE_{σ} [S/m]
CSI w/o ROI limit.	44000	75.8	0.52
CSI w/ ROI limit. (True ROI)	1656	22.1	0.51
CSI w/ ROI limit. (RPM based ROI)	4428	22.0	0.56

to cases without ROI limitation. However, the reconstruction of the conductivity did not show significant improvement with our method. This outcome was consistent with the reasons mentioned in the simulation test detailed in Section III-B-3. It should be noted that since we refer the dielectric property of the water-filled material from [46], there might be difference between the assumed and actual dielectric parameters of the object. However, we can conclude that our proposed initial estimate approach would exclude the possibility that the object is not an air-filled target, and contains some high dielectric contrast material, which should be a reliable basis for decision-making of water leakage.

V. Conclusion

This study presents an experimental investigation for radar prior enhanced inverse scattering analysis for quantitative dielectric profile reconstruction for buried objects into concrete road models, assuming microwave nondestructive applications. The RPM-based radar image could considerably reduce the number of unknowns, thereby enhancing the reconstruction performance of the post-CSI scheme. Furthermore, the initial estimate of the permittivity and conductivity for buried object has been introduced to avoid the local optimal problem. In addition, the relative permittivity of the background concrete media has been automatically optimized by exploiting the focusing response of the rebars, which does not require a preliminary knowledge of the rebar depth and its cover thickness. The numerical and experimental testbed, assuming a real road model with asphalt and floorboard layers, demonstrated that our proposed scheme is effective for more accurate dielectric profile extraction compared to the results without ROI limitation, providing a promising solution for object characterization of high dielectric contrast object, as a water-filled cavity in a concrete road crack, where the data are provided by the commercial radar equipment. Notably, the improvement of the reconstruction accuracy for conductivity was not considerable, compared with that of the permittivity. As a solution for further improving conductivity reconstruction, we plan to introduce the cross-correlated optimization algorithm between relative permittivity and conductivity, focusing on the correlated relation between them. This will help to suppress solution divergence, particularly in the variable for conductivity. Our current project is for extension to the 3-D model to tackle larger scale investigations of real-world road scenarios.

Acknowledgment

The experimental site and operation opportunity have been provided under the cooperation of the Center for Advanced Engineering Structural Assessment and Research, one of the research units of Japan's Public Works Research Institute.

References

[1] M. Fallahpour, J. T. Case, M. Ghasr, and R. Zoughi, "Piecewise and Wiener filter-based SAR techniques for monostatic microwave imaging of layered structures," *IEEE Trans. Antennas Propag.*, vol. 62, no. 1, pp. 282–294, Jan. 2014.

[2] M. Hajebi and A. Hoorfar, "A multiscale optimization technique for large-scale subsurface profiling," *IEEE Geosci. Remote Sens. Lett.*, vol. 18, no. 10, pp. 1706–1710, Oct. 2021.

[3] J. Park and C. Nguyen, "An ultrawide-band microwave radar sensor for nondestructive evaluation of pavement subsurface," *IEEE Sensors J.*, vol. 5, no. 5, pp. 942–949, Oct. 2005.

[4] A. Aljurbua, H. N. Shaman, and K. Sarabandi, "A method for signal leakage cancellation in multistatic subsurface SAR imaging system," *IEEE Geosci. Remote Sens. Lett.*, vol. 19, 2022, Art. no. 3512505.

[5] S. Takahashi and S. Kidera, "Acceleration of range points migration based microwave imaging for non-destructive testing," *IEEE Antenna Wireless Propag. Lett.*, vol. 17, no. 4, pp. 702–705, Apr. 2018.

[6] I. Chernyak and M. Sato, "Near range radar image reconstruction algorithm by weighted envelopes transformation," IEEE Geosci. Remote Sens. Lett., vol. 15, no. 10, pp. 1515–1519, Oct. 2018.

[7] S. Kidera, T. Sakamoto, and T. Sato, "Accurate UWB radar 3-D imaging algorithm for complex boundary without range point connections," *IEEE Trans. Geosci. Remote Sens.*, vol. 48, no. 4, pp. 1993–2004, Apr. 2010.

[8] N. N. Qaddoumi, A. H. El-Hag, and Y. Saker, "Outdoor insulators testing using artificial neural network-based near-field microwave technique," *IEEE Trans. Instrum. Meas.*, vol. 63, no. 2, pp. 260–266, Feb. 2014.

[9] T. S. Yee, N. H. M. M. Shrifan, A. J. A. Al-Gburi, N. A. M. Isa, and M. F. Akbar, "Prospect of using machine learning-based microwave nondestructive testing technique for corrosion under insulation: A review," *IEEE Access*, vol. 10, pp. 88191–88210, 2022.

[10] N. H. M. M. Shrifan, G. N. Jawad, N. A. M. Isa, and M. F. Akbar, "Microwave nondestructive testing for defect detection in composites based on K-means clustering algorithm," *IEEE Access*, vol. 9, pp. 4820–4828, 2021.

[11] L. Chen, L. -Y. Xiao, H. Hu, M. Zhuang, and Q. H. Liu, "Multimodule deep learning scheme for elastic wave inversion of inhomogeneous objects with high contrasts," *IEEE Trans. Geosci. Remote Sens.*, vol. 61, 2023, Art. no. 5910310.

[12] R. Zoughi, *Microwave Nondestructive Testing and Evaluation*. Norwell, MA, USA: Kluwer Academic, 2000.

[13] Y. Gao, M. T. A. Qaseer, and R. Zoughi, "Complex permittivity extraction from synthetic aperture radar images," *IEEE Trans. Instrum. Meas.*, vol. 69, no. 7, pp. 4919–4929, Jul. 2020.

[14] C. Liu, M. T. A. Qaseer, and R. Zoughi, "Permittivity extraction from synthetic aperture radar (SAR) images of multilayered media," *IEEE Trans. Instrum. Meas.*, vol. 70, 2021, Art. no. 8004611.

[15] K. Cho, S. Jo, Y. H. Noh, N. Lee, S. Kim, and J. G. Yook, "Complex permittivity measurements of steel fiber-reinforced cementitious composites using a free-space reflection method with a focused beam lens horn antenna," *Sensors (Basel)*, vol. 21, no. 23, 2021, Art. no. 7789.

[16] G. Govind, N. K. Tiwari, K. K. Agrawal, and M. J. Akhtar, "Microwave subsurface imaging of composite structures using complementary split ring resonators," *IEEE Sensors J.*, vol. 18, no. 18, pp. 7442–7449, Sep. 2018.

[17] Jin-Lin Hu, Z. Wu, H. McCann, L. E. Davis, and Cheng-Gang Xie, "Quasi-three-dimensional method of moments for analyzing electromagnetic wave scattering in microwave tomography systems," *IEEE Sensors J.*, vol. 5, no. 2, pp. 216–223, Apr. 2005.

[18] L. Qu, Y. Yin, Y. Sun, and L. Zhang, "Diffraction tomographic ground-penetrating radar multibistatic imaging algorithm with compressive frequency measurements," *IEEE Geosci. Remote Sens. Lett.*, vol. 12, no. 10, pp. 2011-2015, Oct. 2015.

[19] W. C. Chew and Y. M. Wang, "Reconstruction of two-dimensional permittivity distribution using the distorted born iterative method," IEEE Trans. Med. Imag., vol. 9, pp. 218–225, Jun. 1990.

[20] J. Xiao, X. Tang, B. Liang, F. Han, H. Liu, and Q. H. Liu, "Subsurface reconstruction from GPR data by 1-D DBIM and RTM in frequency domain," *IEEE Geosci. Remote Sens. Lett.*, vol. 17, no. 4, pp. 582–586, Apr. 2020.

[21] H. Liu, Z. Long, C. Qiu, F. Han, and Q. H. Liu, "Reverse-time migration and full wavefrom inversion for subsurface imaging," in *Proc. Prog. Electromagn. Res. Symp.*, Shanghai, China, 2016, pp. 149–149.

[22] P. M. van den Berg and R. E. Kleinman, "A contrast source inversion method," *Inverse Problems*, vol. 13, pp. 1607–1620, Jul. 1997.

[23] S. Sun, B. J. Kooij, and A. G. Yarovoy, "Linearized 3-D electromagnetic contrast source inversion and its applications to half-space configurations," *IEEE Trans. Geosci. Remote Sens.*, vol. 55, no. 6, pp. 3475–3487, Jun. 2017.

[24] R. Marklein, J. Miao, M. Rahman, and K. J. Langenberg, "Inverse scattering and imaging in NDT: Recent applications and advances," in *Proc. Conf.: 9th Eur. Conf. NDT*, 2006, pp. 1–8.

[25] V. Schenone, A. Fedeli, C. Estatico, M. Pastorino, and A. Randazzo, "Experimental assessment of a novel hybrid scheme for quantitative GPR imaging," *IEEE Geosci. Remote Sens. Lett.*, vol. 19, 2022, Art. no. 3510005.
[26] M. Salucci et al., "2-D TM GPR imaging through a multiscaling multifrequency approach in LP spaces," *IEEE Trans. Geosci. Remote Sens.*, vol. 59, no. 12, pp. 10011–10021, Dec. 2021.
[27] A. Desmal and H. Bağcı, "A preconditioned inexact newton method for nonlinear sparse electromagnetic imaging," *IEEE Geosci. Remote Sens. Lett.*, vol. 12, no. 3, pp. 532–536, Mar. 2015.
[28] U. Taşkın and Ö. Özdemir, "Sparsity regularized nonlinear inversion for microwave imaging," *IEEE Geosci. Remote Sens. Lett.*, vol. 14, no. 12, pp. 2220–2224, Dec. 2017.
[29] L. Li, L. G. Wang, F. L. Teixeira, C. Liu, A. Nehorai, and T. J. Cui, "DeepNIS: Deep neural network for nonlinear electromagnetic inverse scattering," *IEEE Trans. Antennas Propag.*, vol. 67, no. 3, pp. 1819–1825, Mar. 2019.
[30] Y. Zhou, Y. Zhong, Z. Wei, T. Yin, and X. Chen, "An improved deep learning scheme for solving 2D and 3D inverse scattering problems," *IEEE Trans. Antennas Propag.*, vol. 69, no. 5, pp. 2853–2863, May 2020.
[31] Z. Wei and X. Chen, "Uncertainty quantification in inverse scattering problems with bayesian convolutional neural networks," *IEEE Trans. Antennas Propag.*, vol. 69, no. 6, pp. 3409–3418, Jun. 2021.
[32] Z. Zong, Y. Wang, and Z. Wei, "A wavelet-based compressive deep learning scheme for inverse scattering problems," *IEEE Trans. Geosci. Remote Sens.*, vol. 60, 2022, Art. no. 2007511.
[33] Y. Chen, H. Zhang, T. J. Cui, F. L. Teixeira, and L. Li, "A mesh-free 3-D deep learning electromagnetic inversion method based on point clouds," *IEEE Trans. Microw. Theory Techn.*, vol. 71, no. 8, pp. 3530–3539, Aug. 2023.
[34] Y. Wang, Z. Zong, S. He, and Z. Wei, "Multiple-space deep learning schemes for inverse scattering problems," *IEEE Trans. Geosci. Remote Sens.*, vol. 61, 2023, Art. no. 2000511.
[35] E. Keeley, J. LoVetri, C. Gilmore, and I. Jeffrey, "Machine-learning-Enabled recovery of prior information from experimental breast microwave imaging data," *Prog. Electromagnetics Res.*, vol. 175, pp. 1–11, 2022.
[36] S. Takahashi, K. Suzuki, T. Hanabusa, and S. Kidera, "Microwave subsurface imaging method by incorporating radar and tomographic approaches," *IEEE Trans. Antennas Propag.*, vol. 70, no. 11, pp. 11009–11023, Nov. 2022.
[37] K. Suzuki and S. Kidera, "Radar enhanced contrast source inversion method for microwave nondestructive evaluation," in *Proc. Int. Symp. Antennas Propag.*, Sydney, Australia, 2022, pp. 223–224.
[38] H. Morimoto, Y. Yamauchi, and S. Kidera, "Contrast source inversion-based multilayered object analysis for terahertz wave imaging," *IEEE Geosci. Remote Sens. Lett.*, vol. 19, 2022, Art. no. 8018005.
[39] N. Otsu, "A threshold selection method from gray-level histograms," *IEEE Trans. Syst., Man, Cybern.*, vol. 9, no. 1, pp. 62–66, Jan. 1979.
[40] A. K. Khambampati, D. Liu, S. K. Konki, and K. Y. Kim, "An automatic detection of the ROI using Otsu thresholding in nonlinear difference EIT imaging," *IEEE Sensors J.*, vol. 18, no. 12, pp. 5133–5142, Jun. 2018.
[41] A. K. Bhandari, A. Singh, and I. V. Kumar, "Spatial context energy curve-based multilevel 3-D Otsu algorithm for image segmentation," *IEEE Trans. Syst., Man, Cybern. Syst.*, vol. 51, no. 5, pp. 2760–2773, May 2021.
[42] M. Ostadrahimi et al., "Analysis of Incident Field Modeling and Incident/Scattered Field Calibration Techniques in Microwave Tomography," *IEEE Antennas Wireless Propag. Lett.*, vol. 10, pp. 900–903, 2011.
[43] A. P. Dempster, N. M. Laird, and D. B. Rubin, "Maximum likelihood from incomplete data via the EM algorithm," *J. Roy. Stat. Soc., Ser. B.*, vol. 39, no. 1, 1977, Art. no. 138.
[44] T. Hanabusa, T. Morooka, and S. Kidera, "Deep-learning-Based calibration in contrast source inversion based microwave subsurface imaging," *IEEE Geosci. Remote Sens. Lett.*, vol. 19, 2022, Art. no. 3006805.
[45] J. Okada and S. Kidera, "Multi-frequency contrast source inversion based permittivity estimation for terahertz multi-layer analysis," *IEEE Trans. Terahertz Sci. Technol.*, vol. 12, no. 5, pp. 535–539, Sep. 2022.
[46] D. G. Archer and P. Wang, "The dielectric constant of water and Debye-Hückel limiting law slopes," *J. Phys. Chem. Reference Data*, vol. 19, no. 2, 1990, Art. no. 371411.
[47] G. González-López, S. Blanch, J. Romeu, and L. Jofre, "Debye frequency-extended waveguide permittivity extraction for high complex permittivity materials: Concrete setting process characterization," *IEEE Trans. Instrum. Meas.*, vol. 69, no. 8, pp. 5604–5613, Aug. 2020.

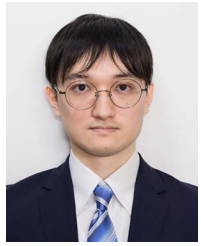

Katsuyoshi Suzuki received the B.E. degree in communication engineering and informatics, in 2021, from the University of Electro-Communications, Tokyo, Japan, where he is currently working toward the M.E. degree in computer and network engineering with the Graduate School of Informatics and Engineering.

His research interest includes inverse scattering and radar signal processing for microwave subsurface applications.

Shingo Nakamura received the M.S. degree in material science and engineering from the interdisciplinary Graduate School of Science and Engineering, Tokyo Institute of Technology, Tokyo Japan, in 2009.

He has been with Fuji Electric Company Ltd., Tokyo, Japan, since 2009. His research interests include the development of sensor devices and measuring instruments based on ultrasonic and electromagnetic technologies.

Shouhei Kidera (Senior Member, IEEE) received the B.E. degree in electrical and electronic engineering, and the M.I. and Ph.D. degrees in informatics from Kyoto University, Kyoto, Japan, in 2003, 2005, and 2007, respectively.

In 2009, he joined as an Assistant Professor with the University of Electro-Communications, Tokyo, Japan, where he is currently a Full Professor with the Graduate School of Informatics and Engineering, University of Electro-Communications, Tokyo, Japan. His research interests include advanced radar signal processing or electromagnetic inverse scattering issue for ultra wideband 3-D sensor or biomedical applications. He has been stayed at the Cross-Disciplinary Electromagnetics Laboratory, University of Wisconsin Madison, Madison, WI, USA, as the Visiting Researcher, in 2016.

Dr. Kidera is a Senior Member of the Institute of Electronics, Information, and Communication Engineers of Japan, and the International Union of Radio Science (Union Radio-Scientifique Internationale), and a Member of the Institute of Electrical Engineering of Japan, and the Japan Society of Applied Physics. He was the recipient of the 2012 Ando Incentive Prize for the Study of Electronics; 2013 Young Scientists Prize by the Japanese Minister of Education, Culture, Sports, Science and Technology; and 2014 Funai Achievement Award, 2022 KDDI Foundation Award, Contribution Award, and 2023 RIEC Award. He was a Principal Investigator of the PRESTO Program of Japan Science and Technology Agency, from 2017 to 2021.